PHILOSOPHICAL TRANSACTIONS B

royalsocietypublishing.org/journal/rstb

Research

Cite this article: Rens EG, Zeegers MT, Rabbers I, Szabó A, Merks RMH. 2020 Autocrine inhibition of cell motility can drive epithelial branching morphogenesis in the absence of growth. *Phil. Trans. R. Soc. B* **375**: 20190386.
http://dx.doi.org/10.1098/rstb.2019.0386

Accepted: 25 May 2020

One contribution of 14 to a theme issue 'Multi-scale analysis and modelling of collective migration in biological systems'.

Subject Areas:
theoretical biology, developmental biology, biophysics, cellular biology

Keywords:
cellular Potts model, epithelial branching, mammary gland, branching morphogenesis, cell-based models, collective cell behaviour

Author for correspondence:
Roeland M. H. Merks
e-mail: merksrmh@math.leidenuniv.nl

†Present address: Department of Mathematics, University of British Columbia, Vancouver, Canada.
‡Present address: Laboratory of Biochemistry, Wageningen University and Research, Wageningen, The Netherlands.
¶Present address: Mathematical Institute and Institute of Biology, Leiden University, Leiden, The Netherlands.

Electronic supplementary material is available online at https://doi.org/10.6084/m9.figshare.c.5025698.

THE ROYAL SOCIETY PUBLISHING

Autocrine inhibition of cell motility can drive epithelial branching morphogenesis in the absence of growth

Elisabeth G. Rens[1,2,†], Mathé T. Zeegers[1], Iraes Rabbers[1,‡], András Szabó[1] and Roeland M. H. Merks[1,2,¶]

[1]Centrum Wiskunde and Informatica, Amsterdam, The Netherlands
[2]Mathematical Institute, Leiden University, Leiden, The Netherlands

EGR, 0000-0001-9274-4469; MTZ, 0000-0003-1742-1189; AS, 0000-0002-8924-038X; RMHM, 0000-0002-6152-687X

Epithelial branching morphogenesis drives the development of organs such as the lung, salivary gland, kidney and the mammary gland. It involves cell proliferation, cell differentiation and cell migration. An elaborate network of chemical and mechanical signals between the epithelium and the surrounding mesenchymal tissues regulates the formation and growth of branching organs. Surprisingly, when cultured in isolation from mesenchymal tissues, many epithelial tissues retain the ability to exhibit branching morphogenesis even in the absence of proliferation. In this work, we propose a simple, experimentally plausible mechanism that can drive branching morphogenesis in the absence of proliferation and cross-talk with the surrounding mesenchymal tissue. The assumptions of our mathematical model derive from *in vitro* observations of the behaviour of mammary epithelial cells. These data show that autocrine secretion of the growth factor TGFβ1 inhibits the formation of cell protrusions, leading to curvature-dependent inhibition of sprouting. Our hybrid cellular Potts and partial-differential equation model correctly reproduces the experimentally observed tissue-geometry-dependent determination of the sites of branching, and it suffices for the formation of self-avoiding branching structures in the absence and also in the presence of cell proliferation.

This article is part of the theme issue 'Multi-scale analysis and modelling of collective migration in biological systems'.

1. Introduction

During the embryonic development of organs such as lungs, kidneys and the mammary gland, epithelial tissues undergo shape changes resulting in a tree-like structure of branches [1,2]. The function of branched organs is to optimize the exchange of chemicals with the surrounding tissue by maximizing the interfacial area. The dynamics of branching from an initially tube-shaped epithelial tissue, called the duct, into the surrounding mesenchymal tissue involves cellular mechanisms such as directed cell migration, oriented cell division, cell shape changes, cell differentiation and cell competition (see reviews [3–5]). The specific process of branching morphogenesis varies per organ, but the key mechanisms are believed to be conserved [6,7]. Although the dynamics of branching in various organs have been characterized well (see for instance, lung [8], kidney [9], mammary gland [10], pancreas [11]), it is still poorly understood what mechanisms drive branching morphogenesis, which of these mechanisms are fundamental, and which ones act on top of the fundamental mechanisms for 'fine tuning'.

Mathematical modelling is a helpful tool to analyse branching morphogenesis. A first class of models asks how biological rules operating on single branches and branch tips can lead to an observed branching pattern. For example, to explain the anatomy of the urinary collecting duct tree, Davies *et al*. [12] have

proposed that the ureteric tubules secrete a hypothetical repulsive factor. The tips of tubules grow towards lower, local concentrations of the repulsive factor at a speed inversely proportional to its concentration. Tubule tips bifurcate once the concentration of the repulsive factor drops below a threshold. The model was used to help explain observed repulsive branch interactions in explants of the collecting urinary duct trees of the mouse kidney, and to plan follow-up experiments. Scheele *et al.* [13] analysed the morphogenesis of the murine mammary gland using a statistical branching model. They constructed trees of which the branches bifurcate or terminate with a near equal probability. This growth process accurately reproduced the distribution of the number of branching levels in the murine mammary gland and the kidney, in support of the potential homology of epithelial branching processes [13]. In a spatially extended variant of this model, growing branches were assumed to terminate as soon as they approached an existing duct, possibly due to TGF-β signalling [14]. This model was able to reproduce observed tissue architecture, such as local densities of branches and directional biases of branch growth. An additional rule stating that approaching branches were repelled by adjacent branches produced better fits with the observed branch density in the kidney.

A second class of mathematical models, which includes the one proposed in this paper, focuses on the cellular and molecular mechanisms responsible for branch tip initiation, branch progression, tip splitting and tip termination. For a long time, it was thought that localized, differential cell proliferation is the main driving factor of branching, but this may not always be true [4]. In the chicken and mouse lung, the buds that initiate new branches form prior to the first appearance of cell proliferation [15,16]. Signalling factors from the mesenchyme have been proposed to drive branching [17]. However, the mesenchyme is not required either, as epithelial tissues can branch in the absence of a surrounding mesenchyme *in vitro* [18–21]. Thus, it is still poorly understood how epithelial tissues branch autonomously in the absence of cell proliferation and mesenchyme. Here we propose a cellular mechanism for such autonomous branching of epithelial tissues.

Epithelial branching has been proposed to be analogous to Laplacian growth, a process that underlies branching in many non-biological systems, including crystal growth [22] and viscous fingering [23]. In a mathematical modelling study of lung morphogenesis, it was proposed that the epithelium branches into the surrounding mesenchyme if the mesenchyme is less viscous than the luminal fluid in the epithelium [24]. In such Laplacian growth processes, the interface of a domain advances with a velocity proportional to the gradient of a field that obeys the Laplacian equation ($\nabla^2 u = 0$), i.e. a field dominated by the diffusion equation, aka the heat equation [25], with $u = 0$ at the interface. Thus points of the morphology located at an interface of positive curvature, which may arise from random deviations from a initially homogeneous boundary, experience a higher gradient of the Laplacian field and will advance faster than the points at flat or concave locations of the interface. This effect is known as the Mullins–Sekerka instability. Instead of pressure and viscosity fields, Laplacian growth dynamics of tissues could also be governed by molecular concentration fields. For example, in the context of tumour branching, it was proposed that cell proliferation depends on the availability of oxygen [26]. Analogously, in a Laplacian growth model of epithelial branching [27], it was proposed that growth is proportional to the local flux of fibroblastic growth factors (FGF).

Other mathematical models have studied in detail how the regulatory interactions between the epithelium and mesenchyme can drive branching. Such epithelial–mesenchymal cross-talk may regulate the highly stereotypic branching patterns of the lung [8] and the kidney [28]. Hirashima & Iwasa [29] studied epithelial–mesenchymal cross-talk in a mathematical model based on the cellular Potts model. They assumed that a deformable epithelial layer is chemoattracted to localized sources of growth factor such as FGF10 or GDNF. This chemotactic mechanism together with cell proliferation produced branches through a buckling mechanism, where the number of branches depended on the ratio between the proliferation rate and the chemotaxis speed [29]. In a further paper, Hirashima *et al.* [30] showed how secretion of SHH by progressing buds can regulate the required localized expression of FGF10 in the mesenchyme. Inhibition of FGF10 expression at high concentrations of SHH, combined with activation of SHH expression at lower concentrations of SHH produce peaks of FGF10 at a small distance from the bud tip. As the tip approaches the lung border, the SHH locally accumulates, leading to a split expression pattern of FGF10. Menshykau *et al.* [31,32] have proposed a model with additional interactions between SHH and FGF10 that could lead to a Turing-type reaction–diffusion mechanism for branching morphogenesis: a positive feedback loop is closed if apart from regulation of FGF10 by SHH, FGF10 from the mesenchyme also induces SHH production in the epithelial cells. The model suggests that the SHH ligand–receptor interactions allow the localized spots to stabilize. By letting the growth rate of the tissue domain depend on the level of ligand–receptor signalling, it was shown that the tissue branches out [33]. Similar Turing mechanisms are thought to be at work in the kidney [34]. All in all this work suggests that an intricate signalling network between the epithelium and mesenchyme generates a pattern of growth factors that drives branching by locally upregulating tissue growth.

Alongside the growth factor interaction network discussed above, evidence has accumulated over the last fifteen years that autocrine inhibitory signals, such as TGF-β provide a robust mechanism for epithelial branching morphogenesis [35–37]. The epithelial cells secrete a diffusive signal which, upon binding, inhibits their own proliferation or their own motility. At convexly curved locations, the inhibitory signal dissipates more easily than at flat or concave locations, much like heat radiates out more rapidly from a mountain peak whereas it gets 'trapped' within valleys. Using tissue-engineered configurations of cells, Nelson *et al.* [35] have shown that murine mammary epithelial cells exhibit such geometry-dependent sprouting activity. Using an image-based model of murine kidney morphogenesis, the Iber group [38] found that a model in which the epithelium secreted an inhibitory signal more robustly and more accurately predicted the future sites of branching than alternative scenarios, such as the Turing-type system discussed above. The Sneppen team [39] showed that the branching growth of *in vitro* cultures of murine pancreatic cells is well explained using a cell-based model in which the autocrine signal inhibits cell proliferation. These mechanisms are analogous to those based on Laplacian growth proposed previously for branching morphogenesis of cell agglomerates [24–27]. However, these models based on proliferation do not explain how epithelia can form branching configurations in the absence of growth, as observed in cell cultures [18–21] and *in vivo* [15,16].

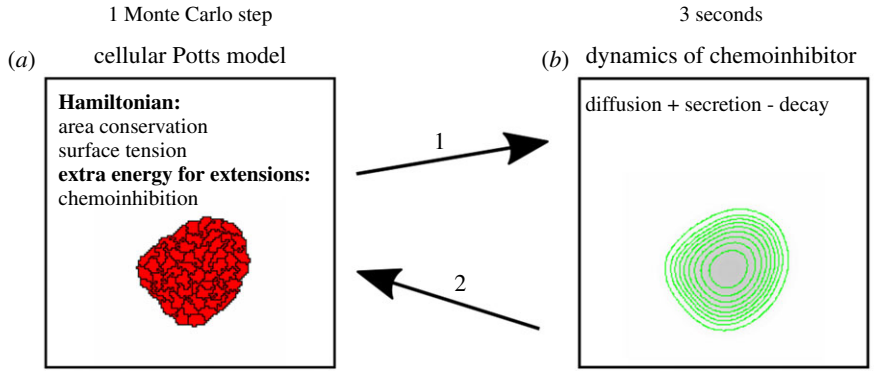

Figure 1. Flowchart of the model. (*a*) CPM calculates cell movement in tissue due to autocrine inhibition; (*b*) autocrine signal is forwarded in space and time, according to PDE in equation (2.4). (Online version in colour.)

Here we introduce a hybrid model based on the cellular Potts model (CPM) and partial-differential equations (PDE) to study if such autocrine inhibition of stochastic cell motility suffices for branching morphogenesis. We assume that the local concentration of an autocrine signal inhibits cell protrusion activity at the boundary of the tissue. We first show that this simple mechanism is a sufficient explanation for the *in vitro* observations by Nelson *et al.* [35]. Then we show that the same mechanism also suffices to reproduce branching morphogenesis in the absence of cross-talk with mesenchymal tissues and in the absence of cell proliferation. Finally we study the behaviour of the model in the presence of proliferation, and show that it suffices to reproduce previously reported behaviour of branch epithelia such as self-avoidance.

2. Results

In vitro observations suggest that cell protrusions are inhibited by the local concentration of TGF-β [35], leading to the hypothesis that diffusion of autocrine TGF-β drives curvature-dependent sites of branching [35]. To test if this mechanism suffices to drive epithelial branching, we developed a hybrid cell based and continuum model (figure 1). A particularly well-suited modelling framework for this purpose is the cellular Potts model (CPM) [40,41]. The CPM naturally represents the stochastistic protrusion and retraction of cells as they were observed in mammary epithelial cell cultures [35]. The CPM also naturally represents the collective migration of cells during branch extension. The CPM (figure 1*a*) simulates the random motility of cells by mimicking iterative attempts to extend and retract pseudopods, e.g. filopodia and lamellipodia. We assume that these cellular extensions and retractions are regulated by a chemoinhibitor, e.g. TGF-β (figure 1*b*). Following Nelson *et al.* [35], we assume that this chemoinhibitor is secreted by the cells, that it diffuses through the extracellular matrix (ECM) in which the cells are embedded, and that it is gradually broken down, e.g. through enzymatic degradation or binding and inactivation in the matrix. The chemoinhibitor inhibits the formation of cellular protrusions in a concentration-dependent manner.

(a) Model description

The CPM describes cells as a collection of lattice sites on a two-dimensional, regular square lattice $\Lambda \subset \mathbb{Z}^2$. Each lattice site $\boldsymbol{x} \in \Lambda$ is assigned a spin or cell identifier $\sigma(\boldsymbol{x}) \in \mathbb{Z}^{\{0,+\}}$, an index of the cell that occupies this lattice site, such that a cell $C(s) = \{\boldsymbol{x} \in \Lambda : \sigma(\boldsymbol{x}) = s\}$, i.e. the set of lattice sites with the same cell identifier s. $C(0)$ represents the medium, i.e. the lattices sites $\boldsymbol{x}$ for which $\sigma(\boldsymbol{x}) = 0$. The system evolves by minimizing a Hamiltonian

$$H = \sum_{(\boldsymbol{x},\boldsymbol{x}')} J(\sigma(\boldsymbol{x}), \sigma(\boldsymbol{x}'))\mathbf{1}_{\sigma(\boldsymbol{x})\neq\sigma(\boldsymbol{x}')} + \lambda \sum_{1\leq s\leq n} (a(s) - A_{\text{target}}(s))^2, \tag{2.1}$$

where $(\boldsymbol{x}, \boldsymbol{x}')$ is a pair of adjacent lattice sites, $J(\sigma(\boldsymbol{x}), \sigma(\boldsymbol{x}'))$ is an interfacial energy, describing cell adhesion and interfacial tensions [42]. $\mathbf{1}_{[\text{expression}]}$ is the indicator function, where $\mathbf{1}_{[\text{expression}]} = 1$ if [expression] is true and $\mathbf{1}_{[\text{expression}]} = 0$ otherwise. The second right-hand-side term introduces a volume constraint, with $a(s) = |C(s)|$, the area of cell s and $A_{\text{target}}(s)$, the target area of cell s and parameter λ is a Lagrange multiplier.

The CPM simulates cell motility through random attempts to retract or extend the cell boundaries. To simulate a random cell extension or retraction, the algorithm iteratively picks a random lattice site $\boldsymbol{x}$, and calculates the energy change ΔH resulting from a copy of $\sigma(\boldsymbol{x})$ into an adjacent lattice site $\boldsymbol{x}'$. It then accepts this copy depending on the change in energy, ΔH, resulting from it, with probability

$$P(\Delta H + H_{\text{work}}) = \begin{cases} e^{\frac{-\Delta H - H_{\text{work}}}{T}} & , \Delta H + H_{\text{work}} \geq 0 \\ 1 & , \Delta H + H_{\text{work}} < 0 \end{cases}. \tag{2.2}$$

T is a motility parameter, aka 'cellular temperature', and represents the amount and magnitude of active, random cell fluctuations, which may act against the passive forces given by the energy H.

H_{work} indicates the energy that is dissipated (e.g. due to friction or viscosity) during a move. It is used here to model chemoinhibition by a field of a secreted chemical, c,

$$H_{\text{work}} = \chi c(\boldsymbol{x}')\mathbf{1}_{\sigma(\boldsymbol{x})>0}\mathbf{1}_{\sigma(\boldsymbol{x}')=0} \tag{2.3}$$

where χ regulates the strength of the inhibition, and $c(\boldsymbol{x}')$ is the chemoinhibitor concentration at the target location $\boldsymbol{x}'$. In the CPM, time is measured in Monte Carlo Steps (MCS), i.e. the number of movement attempts as there are sites in the lattice.

The dynamics of the chemoinhibitory signal is given by a PDE,

$$\frac{\partial c(\boldsymbol{x}, t)}{\partial t} = \underbrace{D\nabla^2 c(\boldsymbol{x}, t)}_{\text{diffusion}} + \underbrace{\alpha \mathbf{1}_{\sigma(\boldsymbol{x})>0}}_{\text{secretion}} - \underbrace{\varepsilon c(\boldsymbol{x}, t)\mathbf{1}_{\sigma(\boldsymbol{x})=0}}_{\text{decay}}, \tag{2.4}$$

where the secretion and decay terms depend on the current state of the CPM. A simulation consists of consecutive steps

Table 1. Default parameter settings.

parameter	description	value	unit	motivation
T	cellular temperature	50	—	chosen followed by sensitivity analysis (figure 6)
A_{target}	target area	50	μm^2	estimated based on nuclear stainings in Nelson *et al.* [35]
χ	chemoinhibition parameter	25	—	chosen followed by sensitivity analysis (figure 5)
λ	area constraint strength	50	—	chosen
D	diffusion coefficient	3.75×10^{-12}	$\mu m^2\ s^{-1}$	chosen together with value of ϵ based on diffusion length reported in Nelson *et al.* [35]
ε	decay rate	5×10^{-3}	s^{-1}	based on half-lives reported in Wakefield *et al.* [44], decay rate in plasma is in range 10^{-4}–10^{-2}; diffusion length $\sqrt{D/\varepsilon}$ matches observations in Nelson *et al.* [35]
α	secretion rate	5×10^{-4}	s^{-1}	estimated
J_{01}	cell–ECM adhesion energy	50	—	estimated to give slightly adhesive cells
J_{11}	cell–cell adhesion energy	20	—	estimated to give slightly adhesive cells
dt	timestep in PDE integrator	0.2	s	numerical stability versus efficiency
dx	pixel size	1×10^{-6}	m	numerical stability versus efficiency
P	PDE iterations per MCS	15	—	numerical stability versus efficiency
t_p	time of increase of area by one lattice site	250	MCS	chosen arbitrarily
A_p	area of division	100	μm^2	estimated

of the CPM and the PDE, where one timestep of the CPM is followed by 3 s of inhibitor dynamics. This time scale was chosen in accordance to our previous work [43]. The parameter values are given in table 1.

(b) Model mimics experimental observation of branching at convex sites

Nelson *et al*. [35] have reported that mammary epithelial cells show geometry-dependent sprouting. They cultured murine mammary epithelial cells inside small micropatterned cavities stamped into collagen gels. After induction with growth factors, the cells formed multicellular sprouts preferentially at the positively curved (convex) parts of the cell clusters (figure 2*a*,*b*). At crevices between two cell clusters, where a secreted growth factor would accumulate, no sprouts formed (figure 2*c*,*d*). To test if our mathematical model suffices for explaining these observations, we initialized our model simulations with the shapes used in the experiments by Nelson *et al.* [35] (figure 2*e*–*h*). The size of the geometry matched those used in the *in vitro* experiments [35] and we used the parameters in table 1, for which there are on average five cells across the diameter, corresponding to nuclei counts in Nelson *et al*. [35].

We first ran the CPM model for 750 MCS during which time cell shapes could equilibrate. For the next 750 MCS, we simulated only the PDE such that the chemical field approached a steady state (figure 2*i*). The shapes and lengths of these simulation steady-state gradients matched well with the experimentally observed TGF-β (compare fig. 4A in [35] with figure 2*i*). We then simulated the CPM and the PDE concurrently for a further 4000 MCS, allowing for some cell expansion (1 μm^2 of additional target area per 100 MCS), but disabling cell division. Frequency maps show the percentage of the last 4000 MCS that a cell is present at the site. Similar to the *in vitro* observations [35], *in silico* multicellular sprouts appeared preferentially at the convex parts of the geometry. For the 'C' shape, branching occurs at the tips and the 'belly' of the 'C', which are the convex parts (figure 2*e* and electronic supplementary material, video S1). Similarly, for the 'Y' shape, sprouts appeared around the convex tips (figure 2*f* and electronic supplementary material, video S2). Our model could also reproduce the setup shown in figure 2*c*,*d*. Here cells were placed into two rectangular wells positioned at 90° angles or adjacent to each other. As in the C- and Y-shaped geometries, the cells sprouted at the convex regions of the morphologies away from the other morphologies (figure 2*g*,*h* and electronic supplementary material, videos S3 and S4). No sprouts were formed at the convex regions near the crevice between the two geometries due to accumulation of the inhibitory signal (red curve in figure 2*i*). This observation is correctly reproduced in the simulations.

A discrepancy between the predictions of our simulations and the experimental observations is that we needed to keep a bit of pressure on the cell boundaries through a slow cell expansion term. In the absence of this term, the concave cell boundaries moved inwards, as can still be observed in figure 2*g*,*h*; a more refined representation in the CPM of the 'cavities' that contained the cells in the experiments will likely prevent this inward motion and hence improve the predictions. Possibly this also solves a further discrepancy with the experiments: the cell expansion term generates sites of cell protrusion that are not seen in the experiments (e.g. see the lateral protrusions adjacent to the crevice in figure 2*h* and the lateral protrusion below the 'fork' of the Y in figure 2*f*).

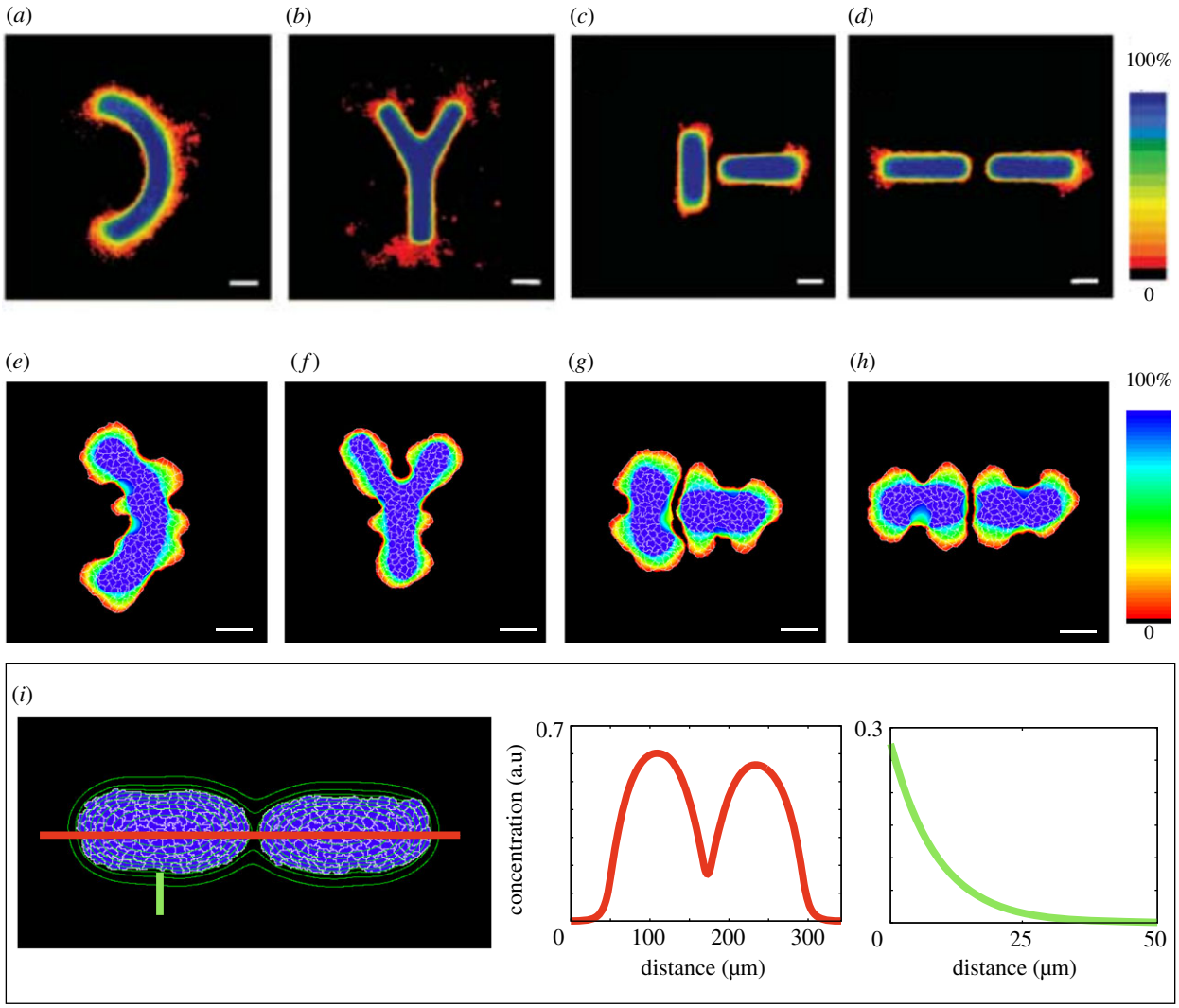

Figure 2. Model replicates branching at convex sites of geometries. Heat map indicates the percentage of time a cell was present at a given site during 4000 Monte Carlo Steps. (*a*) Experimental frequency map of epithelial cells for the reversed 'C' shape; (*b*) experimental frequency map of epithelial cells for the 'Y' shape; (*c*) experimental frequency map of epithelial cells in two orthogonally placed rectangles; (*d*) experimental frequency map of epithelial cells in two aligned rectangles; (*e*) simulated cells placed in a reversed 'C' shape—see also electronic supplementary material, video S1; (*f*) simulated cells placed in a 'Y' shape—see also electronic supplementary material, video S2; (*g*) simulated cells placed in two orthogonally placed rectangles—see also electronic supplementary material, video S4; (*h*) simulated cells placed in two aligned rectangles—see also electronic supplementary material, video S3; (*i*) concentration profiles of the inhibitory, autocrine signal for the simulation shown in panel (*h*). Panels (*a–d*) reprinted from Nelson *et al.* [35] with written permission from the AAAS (#4680251276893). Parameter values for the simulations as in table 1. Scale bars: 50 μm. (Online version in colour.)

(c) Autocrine inhibition of cell movement drives branching

We next asked if this mechanism proposed in Nelson *et al.* [35] also suffices for branching morphogenesis. We initiated the model simulation with a disc-shaped structure of radius 0.225 mm in a lattice of 0.9 mm by 0.9 mm containing approximately 1000 cells. Figure 3*a* and electronic supplementary material, video S5 show a model simulation for the first 9000 MCS. A first look at the time series of the simulation shows that after approximately 1000 MCS the boundary of the disc becomes bumpy. Then around 3000 MCS, many droplet-like extensions appear. The length of these extensions increase and, as a result, a fully branched structure, with evenly thick branches is formed, that stabilizes around 8000 MCS. To test if and to what extent this result depends on the numerical resolution and scaling of the simulation (Δx), we have repeated it for $\Delta x = 5 \times 10^{-7}$ m (electronic supplementary material, video S6) and for $\Delta x = 2.5 \times 10^{-7}$ m (electronic supplementary material, video S7), i.e. twice and four times the original resolution. At these refined resolutions, the simulations progressed more slowly due to the reduced length scale of the cellular extensions and retractions, but otherwise the results did not depend on the spatial resolution. We thus performed our parameter studies at $\Delta x = 1 \times 10^{-6}$ m for computational efficiency.

To quantify branching, we define the compactness of the morphology as $C = A_{\text{tissue}}/A_{\text{hull}}$ [43], i.e. the ratio between the area of the largest connected component of the tissue and the area of its convex hull, the smallest convex polygon that contains the tissue [45]. A compactness of 1 implies a perfectly circular tissue shape, whereas a low value of compactness indicated a high degree of branching or high degree of cell scattering. The compactness of the morphology rapidly drops during the first 5000 MCS and slowly decreases after that (figure 3*b*) indicating slow thinning of the branches.

Initially, the boundary of the circular tissue roughens due to random cell motility. While the secreted inhibitor accumulates at the concave locations of the morphology, it diffuses away more easily at the convex locations (figure 3*a*). As a result, cell motility is inhibited more strongly at the concave and flat

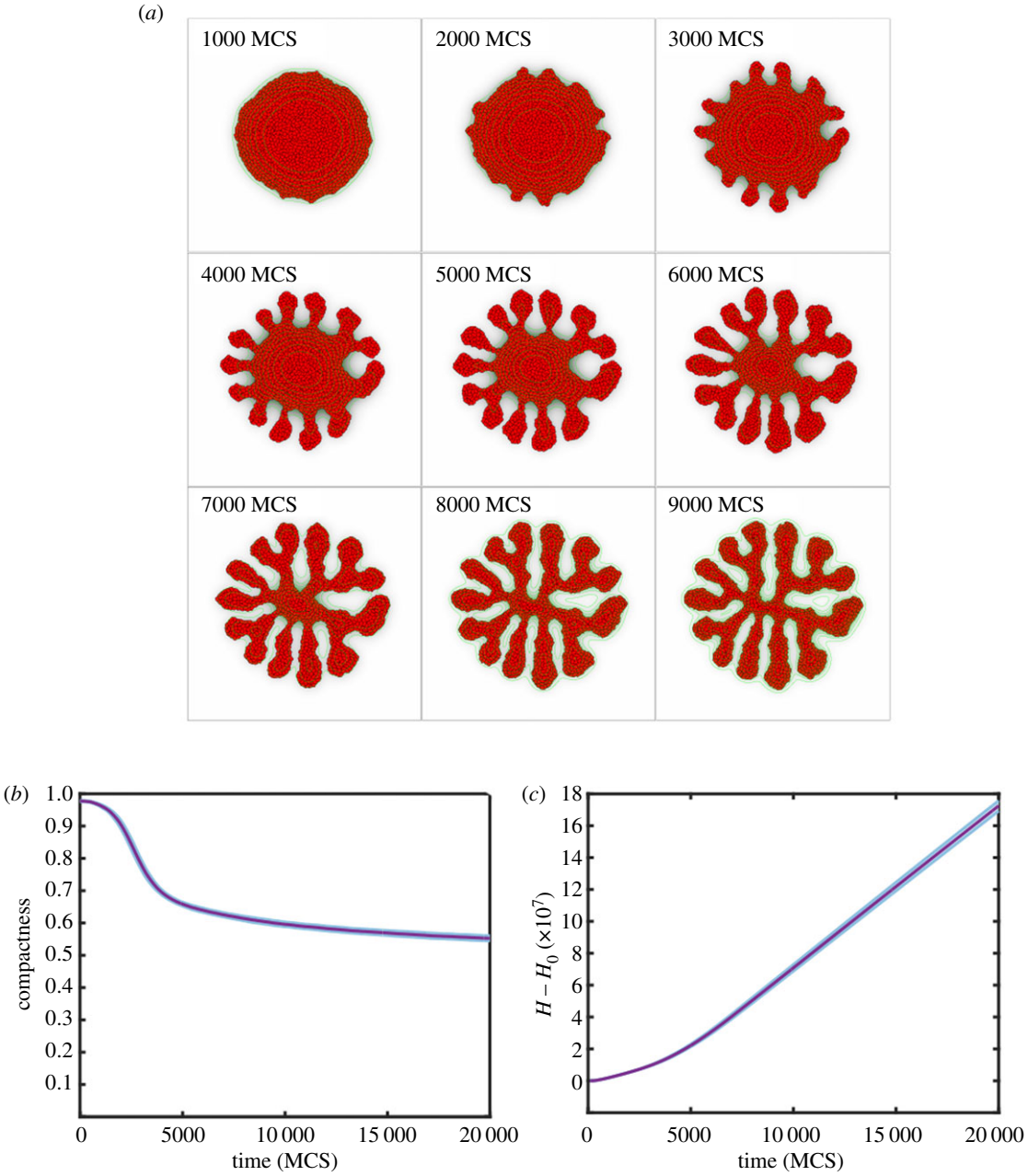

Figure 3. Simulation of branching by autocrine inhibition. (*a*) Timelapse of a model realization—see also electronic supplementary material, video S5; (*b*) compactness as a function of time; shaded regions, standard deviations of 100 simulations; (*c*) energy spend by the system ($H - H_0 = \sum \Delta H$) as a function of time; shaded regions, standard deviations of 100 simulations. (Online version in colour.)

regions than at the convex regions of the morphology, such as the branch tips. Thus the secreted inhibitor leads to a geometry-dependent rate of cell extension. Cell motility is strongly inhibited at the 'valleys' between the branches, but is more frequent at the sprout tips. This leads to a 'ratchet'-type, dissipative branching mechanism: cells attempt to extend and retract randomly, and at sufficiently high temperatures they can do so even against the local energy gradient generated by the inhibitor (equation (2.2)). Because the secreted inhibitor dissipates at branch tips, such extensions against the energy gradients are more frequent at branch tips than in the 'valleys'. To test if indeed branching is due to such a 'ratchet'-like, dissipative mechanism, we measured the cumulative energy of the system $H_{\mathrm{cum}}(t) = H(t) - H(0) = \sum_{i=0}^{i=t} \sum_{\mathrm{MCS}} (\Delta H + H_{\mathrm{work}})(i)$, where $\sum_{\mathrm{MCS}}$ is the sum over all the accepted copy attempts with a Monte Carlo Step. Indeed H_{cum} increases as a function of time (figure 3*c*), showing that for many of the moves $\Delta H > 0$ holds. Thus many of the moves act against a large positive energy contribution H_{work}, which is due to the inhibition of cell motility (equation (2.4)).

(d) Random motility regulates branch initiation and branching speed

The previous section showed that the proposed branching mechanism is driven by random cell motility. Interestingly, Btbd7, a positive regulator of epithelial cell motility, is required for branching morphogenesis of salivary glands and the lung [46], and is expressed in branching end buds in a variety of branching epithelial organs [47]. Knock-out of Btbd7 reduces epithelial cell motility in the end buds of submandibular salivary glands, leading to incomplete branching [47]. We thus hypothesized that the level of random cell motility should have similar effects in our mathematical model. The distribution of the magnitudes of the random forces exerted by the cell extensions and retractions is given by parameter *T*,

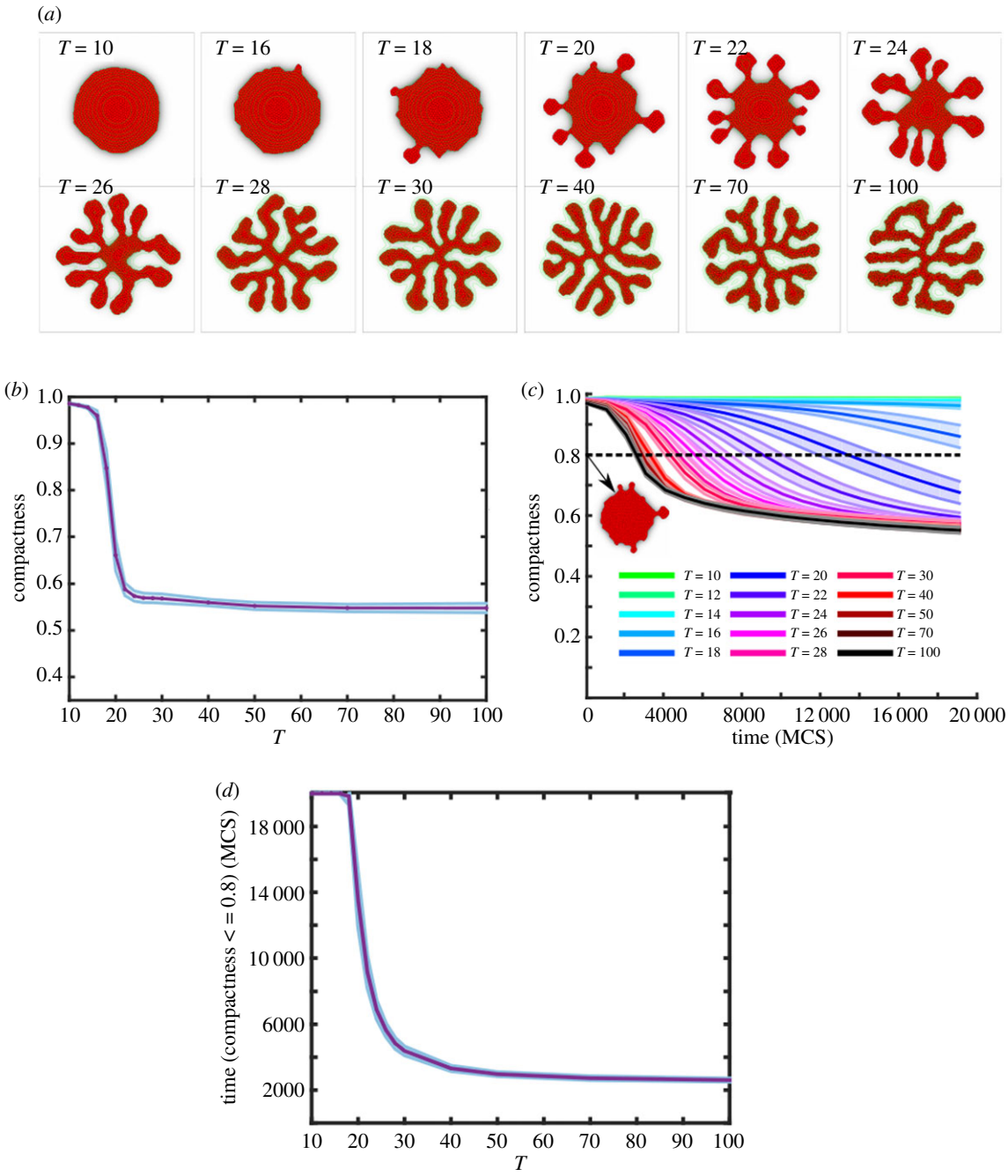

Figure 4. Cellular temperature regulates branching dynamics. (*a*) Example configurations of the tissue at 20 000 MCS for different values of *T*; (*b*) compactness as a function of *T*; shaded regions, standard deviations of 100 simulations; (*c*) compactness as a function of time; shaded regions, standard deviations of 100 simulations; different colours, different values for *T*, see legend (Online version in colour.)

the motility parameter, aka cellular temperature (equation (2.2)). Figure 4*a* shows morphologies for increasing values of *T*. Consistent with the inhibition or knockout of Btbd7 [46,47], at low values of *T* the tissue did not branch, because only a few random cell protrusions were strong enough to overcome the effect of the chemoinhibitor. For slightly higher cell motility, at cellular temperatures of around $T = 20$, the tissue developed droplet-like extensions: as soon as one or a few protrusions locally overcame the effect of the inhibitor the curvature locally increased leading to reduced levels of chemoinhibition. For elevated values of *T*, the tissue branched normally and the branches became longer and thinner than for lower values of the cellular temperature. Indeed the compactness of the morphologies formed after 20 000 MCS declined sharply for increasing values of *T* up to around $T = 20$ (figure 4*b*), reflecting that branching occurs from around $T = 20$. Figure 4*c* shows the compactness as a function of time for increasing values of *T*. For low values of *T* ($T = 18$ and $T = 20$), the compactness decreased slowly over time, but it did not reach a low compactness before the end of the simulation, while for higher values of *T* branching accelerates. We quantified speed of branching by measuring $t(C = 0.8)$, the time required for the tissue to drop below a compactness of 0.8 (dashed line in figure 4*c*). Figure 4*d* shows that the speed of branching quickly increases with the value of *T* and then saturates. In conclusion, consistent with experimental observation, the motility parameter *T* regulates the initiation and the speed of branching and has a small effect on branching morphology.

(e) Strength of autocrine inhibition has a biphasic effect on branching

The previous section showed how the cellular temperature affected branching dynamics. We next studied the effect of

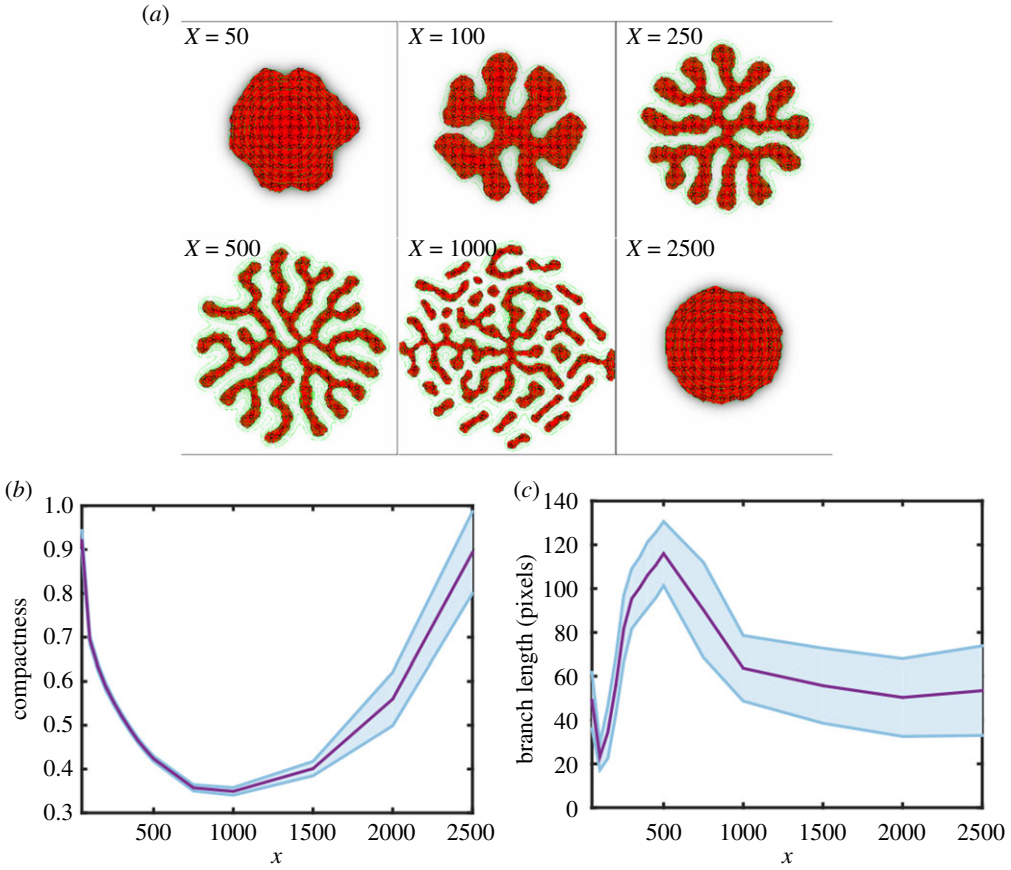

Figure 5. Strength of autocrine chemoinhibition biphasically drives branching. (*a*) Example configurations of the tissue at 20 000 MCS for different values of χ; (*b*) compactness as a function of χ; shaded regions, standard deviations of 100 simulations; (*c*) branch length as a function of χ; shaded regions, standard deviations of 100 simulations. (Online version in colour.)

the chemoinhibition strength χ. Because the value of χ and T both determine the probability that a cellular protrusion is accepted (see equations (2.2) and (2.3)), the effect of χ and T are likely interrelated. Interestingly, the chemoinhibition strength (figure 5*a*,*b*) has a biphasic effect on branching. For relatively low values of $\chi = 50$, the morphology retained its circular shape and no branches formed or they remained very short(figure 5*c*; the increased values of the branch length for low values of χ in figure 5*c* are due to artefacts of the skeletonization algorithm). For these low values of χ the impact of the autocrine signal was negligible, such that the dynamics was dominated by the 'standard' Hamiltonian (equation (2.1)). At higher values of χ, the response to the autocrine inhibitory signal differed to a sufficiently large extent between concave and convex regions, such that the curvature effect set in and branches formed, as shown by the reduced compactness (figure 5*b*) and increased branch length (figure 5*c*). At even higher values of χ, the branches became thinner and longer. As the chemoinhibition is active only at cell–ECM interfaces, at higher values of χ the chemoinhibition term became dominant over the other components of the Hamiltonian including the surface tension. This also allowed droplets to break off from the spheroid; this is an irreversible process, because the chemoinhibitory field made it energetically costly for such droplets to join the morphology again. For the largest values of χ tested, branches did not form, because cell protrusions became very costly. In conclusion, the chemoinhibition strength χ regulates the degree of branching in a biphasic manner.

(f) Decreasing surface tension promotes branching

In a study where lung epithelium was isolated *in vitro*, Hartmann & Miura [27] showed that a decrease in surface tension, by disruption of the cytoskeleton using cytochalasin D, results in more but smaller branches. Similarly, inhibiting cell contractility, thus reducing surface tension, promotes branching morphogenesis of the pancreas [19]. We therefore studied how the value of surface tension affected branching morphogenesis. In the CPM, surface tension γ_{01} is defined as $\gamma_{01} = J_{01} - (J_{11}/2)$ [40], where J_{01} is the interfacial energy between cells and medium and J_{11} is the interfacial energy between two cells. Figure 6 shows the effect of γ_{01} on branching morphogenesis. In agreement with the experimental data, increasing the surface tension reduced the number of branches and yielded thicker branches. For very low values of γ_{01} many thin branches appeared, which occasionally merged with one another. In simulations with increased surface tension the branches became thicker (figure 6*b*) and shorter (figure 6*c*). For the highest values of γ_{01} tested, the branches became droplet-shaped and had more variable thickness than for lower values of γ_{01}. In agreement with Hartmann & Miura [27], these results illustrate that the surface tension γ_{01} acts as a restoring force that counteracts the curvature effect due to chemoinhibition.

(g) Space-filling branching growth and branch avoidance in, presence of cell proliferation

The results above suggest that autocrine inhibition of random cell protrusion is sufficient for branching morphogenesis of epithelial cells, even in the absence of cell proliferation and the of

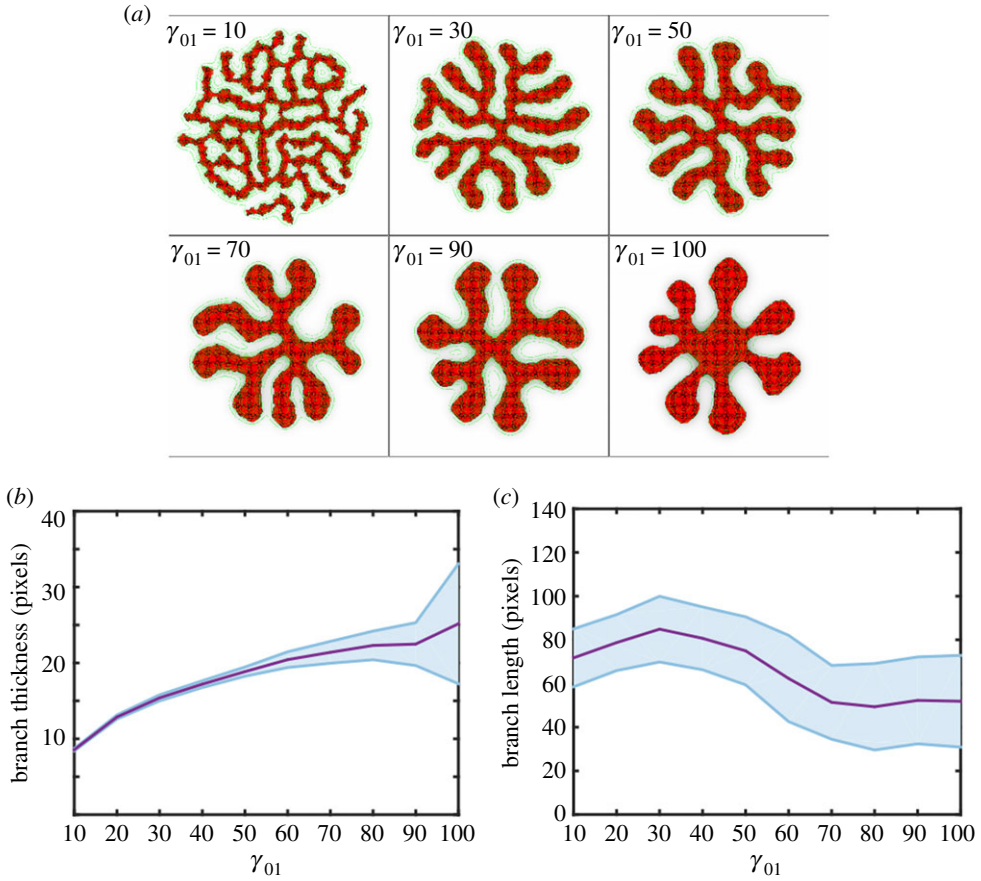

Figure 6. Surface tension affects branch morphology. (*a*) Example configurations of the tissue at 20 000 MCS for different values of J_{01}; (*b*) branch thickness as a function of γ_{01}; shaded regions, standard deviations of 100 simulations; (*c*) branch length as a function of γ_{01}; shaded regions, standard deviations of 100 simulations. (Online version in colour.)

regulatory interactions with the mesenchyme. However, *in vivo* branching morphogenesis usually requires cell proliferation [18]. Therefore, we next investigated how the proposed branching morphogenesis mechanism behaved in the presence of cell proliferation. To mimic cell proliferation, the target area was incremented by 1 once every 100 MCS. Cells divided over their short axis after the actual area had reached a threshold value; thus pressure from adjacent cells inhibited proliferation.

Figure 7 and electronic supplementary material, video S8 show a simulation initiated from a circular blob of proliferative cells. The insets in the final configuration highlight two proliferation events (purple and cyan dots). With proliferation, the mechanism produced a space-filling branching structure. The branches did not merge: branch tips that grew towards each other were repelled by one another (figure 7; black circle) or they were terminated. Such 'self-loathing' [48] of branches is due to the accumulation of the autocrine inhibitor between branches (figure 2*g*,*h*) and has been observed in *ex vivo* cultures of murine urinary collecting ducts [12] and mammary gland tissue [14]. Note that in our model, the auto-inhibition is responsible for the branching morphogenesis itself, and also gives rise to 'self-loathing' [48] of adjacent branches, leading to branch avoidance.

3. Discussion

Using mathematical modelling we have shown that the mechanism for geometry-dependent sprouting in tissue-engineered constructs of mammary epithelial cells proposed by Nelson *et al*. [35] suffices for autonomous branching morphogenesis of epithelial tissues, in the absence of cell proliferation and interaction with the surrounding mesenchymal tissues. Importantly, and in contrast to related models based on Laplacian growth principles, the present model produces sprouts and branching structures in the absence of proliferation. The model suggests that branching morphogenesis can occur due to a 'ratcheting' mechanism, which favours random cellular protrusions at convex locations of the morphology over protrusions at concave locations. The present model derives conceptually and methodologically from our previous work on angiogenesis [43], in particular from the model variant based on 'extension-only chemotaxis' (see § 'A Dissipative Sprouting Mechanism' in Merks *et al.* [43]). The key difference with this previous work is that the autocrine *chemoinhibition* mechanism studied here is based on the *concentration* of $c(\boldsymbol{x})$ (equation 2.3), whereas the chemotactic mechanisms studied previously relied on chemical gradients $\nabla c(\boldsymbol{x})$. This small difference has a large effect on the patterns predicted by the model: the present mechanism explains the formation of self-avoiding branching patterns, as observed in many epithelial-derived branching organs, whereas the previous work predicted the formation of network-like patterns, such as those found in microvasculature. In the presence of proliferation our model is similar to previous models based on Laplacian growth. In these models, tissues branch due to a Mullins–Sekerka instability, where positive curvatures experience higher gradients of a pressure field [24], a growth-promoting [27] or a growth-inhibiting field [39]. In particular, the latter model by the Sneppen group [39], which is based

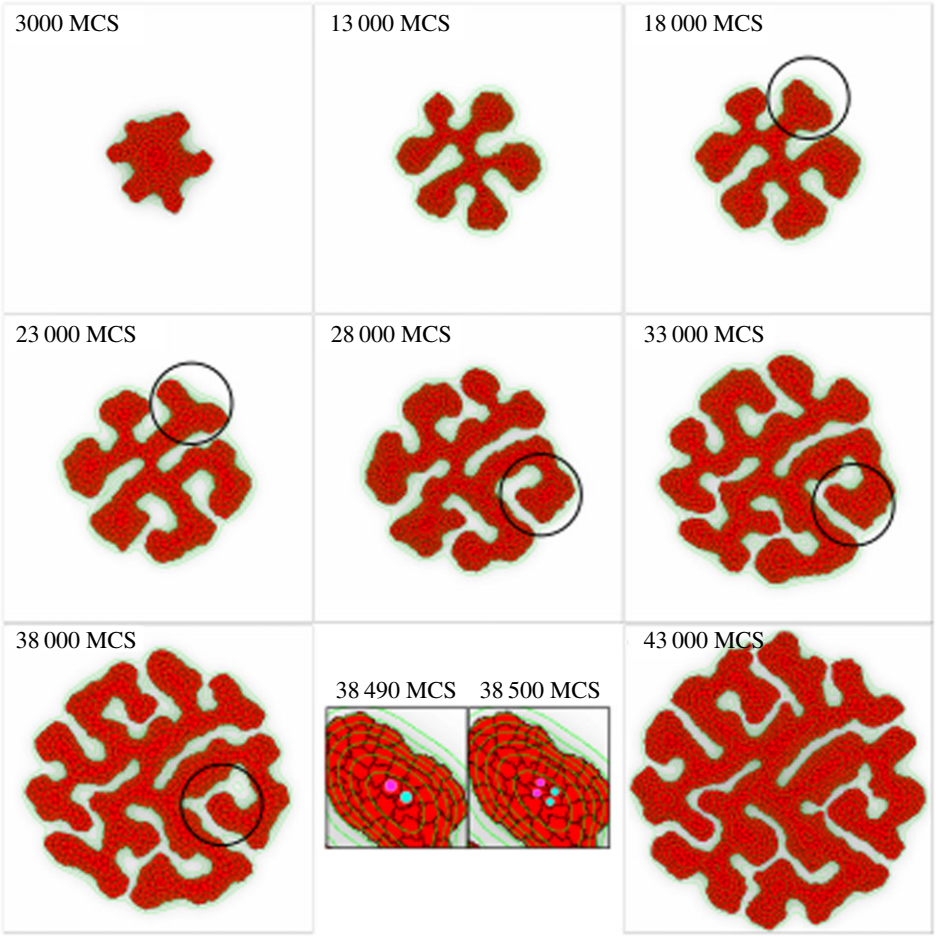

Figure 7. Branching with cell proliferation. Timelapse of a model realization with proliferation; see also electronic supplementary material, video S8. The black circle tracks a branch avoidance event. The inset at 15 500 MCS shows two cell division events. (Online version in colour.)

on growth-inhibition, resembles ours. However, our model differs from it in an essential aspect: our model can explain branching morphogenesis in absence of proliferation.

The assumptions of the model are simple, but plausibly based on experimental observation [35], and its predictions agree surprisingly well with some observations of branching epithelial organs. At the same time, there are of course many observations that our model cannot explain and that will open up new perspectives for future modelling studies. In particular, observations of renal epithelial cells challenge the hypothesis of autocrine inhibition of motility studied in this work [49]. Renal epithelial cells grown on micropatterns of specific curved geometry exhibit curvature-dependent protrusions. These are potentially regulated by autocrinically secreted BMP7, a member of the TGF-β superfamily. To test this hypothesis, Martin *et al.* [49] applied a flow to the culture medium that should flush away any diffusive signals potentially secreted by the cells. Surprisingly, this treatment did not affect the curvature-dependent protrusions. The authors suggested that membrane tension might be responsible for the curvature effect instead. Pavlovich *et al.* [36] argued that the autocrine inhibition mechanism may uniquely apply to mammary epithelial patterning. An alternative explanation for the observations by Martin *et al.* [49] may be that autocrinically secreted signals are bound to secreted ECM proteins, which would prevent them from being flushed away. Such pericellular retention of signalling molecules has been observed for VEGF in endothelial cells [50]. Indeed the activity of TGF-β activity is likely regulated by the chemistry and the mechanics of the ECM. TGF-β is bound to the ECM in a latent form. The active moiety can be released from the ECM through proteolysis [51] or through mechanical stretching of TGF-β [52]. Further supporting the importance of the ECM in branching morphogenesis, reducing the cytoskeletal tension (likely reducing the cellular traction forces exerted on the ECM) reduces the number of branches formed in embryonic lung explants [53,54]. In our previous work, we have modelled how TGF-β release from fibrin matrices can regulate angiogenic sprouting [55], and how mechanical cell–ECM interactions can coordinate pattern formation and sprouting in endothelial cell cultures [56,57]. In our ongoing studies, we are incorporating these two approaches into our models of epithelial branching. These model extensions may provide deeper insight into the role of the ECM in branching morphogenesis. Apart from the leads provided by the observations of Martin *et al.* [49], another direction for further research may consider TGF-β release through ECM proteolysis and mechanical straining of the ECM by the epithelial cells. Possibly such models of the mechanochemical cross-talks in TGF-β signalling can help reconcile some of the experimental observations on the role of membrane tension and mechanical force generation in branching morphogenesis.

Another lead that may provide new insights into branching morphogenesis concerns the analogy with scratch assays for wound healing. In such assays, epithelial cells migrate into a free surface left open by the scratch [58,59]. During closing of the scratch, the epithelial cells organize into finger-like structures, which will eventually merge to close the free space.

The finger-like structures extending from the boundary look similar to initial branching structures, and like in branching, proliferation does not seem to be the driving factor in fingering experiments [58] nor in mathematical models of fingering [60,61]. With a cellular Potts model, Ouaknin *et al.* [60] showed that if cells in contact with free space secrete a signal to which all cells chemotact, fingering into the open space occurs. In this model, cells at the boundary move and drag cells along, which will encounter more open space which increases the chemotactic signal and thus reinforces fingering. In a model by Mark *et al.* [62], the Mullins–Sekerka instability arises from a curvature-dependent cell motility. In a follow-up paper which included velocity alignment of cells [61], it was shown that the thickness of the fingers depends on the length scale on which the cells in the bulk align their velocities. Indeed, epithelial cells in fingers are observed to move together in a highly coordinated fashion [59]. The relationship between motility and curvature was based on observations where epithelial cells have a higher protrusion rate at convexly curved surfaces [63].

For computational efficiency, the analyses in this work are based on two-dimensional simulations. However, it is straightforward to extend the model to three dimensions (see electronic supplementary material, video S9 for a three-dimensional example with proliferation). Our two-dimensional simulations represent quasi-two-dimensional cultures, e.g. mammary epithelial in thin fibrin gels [64] or kidney rudiments cultured on filters supported by Trowell screens [12]. To represent such quasi-two-dimensional situations, we have assumed that the decay of the autocrine signal only takes place outside of the cells and the signal only affects cell motility at the periphery. An alternative interpretation of a two-dimensional model could be the projection of the three-dimensional case in two dimensions. In this interpretation of the two-dimensional model, we should also consider the degradation of the signal underneath the cells.

The present model is of course a great simplification of epithelial branching morphogenesis *in vivo*. Epithelial morphogenesis involves interactions of many signalling molecules and receptors from the epithelium and mesenchyme and, despite some similarities, there are large differences between organs of epithelial origin. The model generates variable branching patterns such as in mammary epithelial tissues [13,14], whereas other organs such as lung and kidney display highly stereotypic, reproducible patterns of branching [8,28]. Future work could explore the hypothesis that additional signalling molecules and the interaction with the surrounding mesenchyme and the ECM could fine-tune generic branching mechanisms such as the one presented here, leading to more stereotypical branching.

4. Methods

(a) Model implementation

The model was implemented using the Tissue Simulation Toolkit (http://sourceforge.net/projects/tst). The PDE is solved by using a forward Euler method on a regular square lattice matching that of the CPM. i.e. $\Delta x = 2$ µm. The CPM and PDE are coupled using an operator splitting approach: after running the CPM for one Monte Carlo step, 15 of the numerical integration steps are performed with $\Delta t = 0.2$ s, such that the PDE runs for $t_c = 3$ s per MCS. As initial conditions for the PDE, we assume

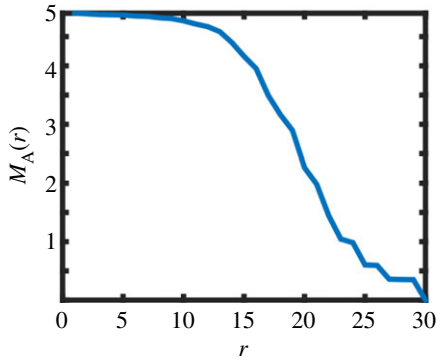

Figure 8. Example of the radius r of a branching morphology as a function of the area of the morphological opening $a \circ b(r)$. (Online version in colour.)

$c(\boldsymbol{x}, 0) = 0$ for all $\boldsymbol{x}$. We used zero boundary conditions, i.e. $c(\boldsymbol{x}, t) = 0$ at all boundaries.

(b) Morphological measures

The morphologies were characterized using the following morphometric measures.

(i) Compactness

The compactness is defined as the ratio between A, the domain covered by the tissue, and the area of its convex hull A_{hull} [45]:

$$C_{\text{comp}} = \frac{A_{\text{tissue}}}{A_{\text{hull}}}. \tag{4.1}$$

The convex hull is the smallest convex polygon that encloses the object of interest. A compactness of $C_{\text{comp}} = 1$ indicates a convex tissue shape, whereas a lower value of the compactness indicates branching or cell scattering.

(ii) Branch length

In order to find the branches of the structure, we generate the morphological skeleton of the tissue [65,66]. Using this skeleton image, we calculate the length of the branches as follows. For every edge, the two nodes of the edge are removed from the skeleton image by removing all lattice sites around the nodes with increasing radius, until a radius w is found such that the skeleton image is divided into at least two separate components, of which one is the edge of interest. The length of a branch is then determined by counting the pixels that make up the branch and adding twice the radius w to the final result.

(iii) Branch thickness

To calculate branch thickness, we adopted an approach by Filatov *et al.* [67]. We take a to be the image of the tissue and let $b(r)$ be a disc $b(r) = \{(x, y) \in \mathbb{R}^2 : x^2 + y^2 \leq r\}$ with variable radius r. The branch thickness can now be defined as the value of r for which branches disappear out of the morphological opening $a \circ b(r)$.

The area of the morphological opening decreases with the radius r (figure 8), because more branches disappear from the image with increasing r. We approximate the branch thickness by finding a point where this graph decreases sufficiently fast and then becomes flat, indicating that most branches have disappeared. At some point the graph becomes more or less horizontal. This region corresponds to the circular part of the tissue, in which many circles $b(r)$ fit. So, the value for r for which the graph becomes horizontal indicates the thickness of the branches. We detect this horizontal region by first finding a region where the graph decreases sufficiently fast and then a region where it decreases slowly. Let $M_A(r)$ be the area of $a \circ b(r)$. We find an $0 < r_1 \leq r_{\max}$ for which $M_A(r_1) - M_A(r_1 - 1) < a_1$ and then the value $r_1 < r_2 \leq r_{\max}$ for

which $M_A(r_2) - M_A(r_2 - 1) > a_2$ (r_2 is set to r_{max} if such a value does not exist). The branch thickness is then found by taking the value of r for which $M_A(r)$ is closest to $\frac{1}{2}(M_A(0) + M_A(r_2 - 1))$. The values of a_1 and a_2 are determined empirically. The value of r_{max} is set to 30 to reduce computation time.

In case no branches or only very small branches are present ($M_A(r_1) - M_A(r_1 - 1) \geq a_1$ for all $0 < r_1 \leq r_{max}$) we apply the following algorithm. When the decrease in $M_A(r)$ is not larger than $-a_1$ in the entire graph we simply take the distance from the centre of mass of the tissue to an ECM point in four different directions and select the lowest distance as the radius. In this case, the radius represents the radius of the unbranched cell aggregate but we take this as the branch thickness. We follow this approach, because increasing the radius to the width of the initial circular tissue (typically more than twice as large as $r_{max} = 30$) and repeatedly computing $M_A(r)$ would require excessive computation time.

Data accessibility. The simulations have been performed with a version of the Tissue Simulation Toolkit (https://sourceforge.net/projects/tst/).

Authors' contributions. E.R. drafted the manuscript and helped coordinate the study. M.Z. carried out the computer simulations and designed and performed the analyses and helped draft the manuscript. I.R. drafted an early version of the manuscript, performed preliminary simulations and designed and carried out the three-dimensional simulation. A.S. helped design the study and helped draft an early version of the manuscript. R.M. conceived of the study, designed the study, coordinated the study, carried out computer simulations and helped draft and critically revised the manuscript. All authors gave final approval for publication and agree to be held accountable for the work performed therein.

Competing interests. We declare we have no competing interest.

Funding. This work is part of the research programme NWO Vidi with project number 864.10.009 and NWO Vici with project number 865.17.004 to RM, which is (partly) financed by the Dutch Research Council (NWO). This work was cofinanced by the Netherlands Consortium for Systems Biology (NCSB), which was part of the Netherlands Genomics Initiative/Netherlands organization for Scientific Research. During the completion of this manuscript, EGR was supported by a Natural Sciences and Engineering Research Council (Canada) Discovery grant to Leah Edelstein-Keshet. This work was carried out on the Dutch national e-infrastructure with the support of SURF Cooperative. The funders had no role in study design, data collection and analysis, decision to publish, or preparation of the manuscript.

References

1. Davies J. 2005 *Mechanisms of morphogenesis: the creation of biological form*. Amsterdam, The Netherlands: Elsevier.
2. Horowitz A, Simons M. 2008 Branching morphogenesis. *Circ. Res.* **103**, 784–795. (doi:10.1161/CIRCRESAHA.108.181818)
3. Ochoa-Espinosa A, Affolter M. 2012 Branching morphogenesis: from cells to organs and back. *Cold Spring Harb. Perspect. Biol.* **4**, a008243. (doi:10.1101/cshperspect.a008243)
4. Varner VD, Nelson CM. 2014 Cellular and physical mechanisms of branching morphogenesis. *Development* **141**, 2750–2759. (doi:10.1242/dev.104794)
5. Wang S, Sekiguchi R, Daley WP, Yamada KM. 2017 Patterned cell and matrix dynamics in branching morphogenesis. *J. Cell Biol.* **216**, 559–570. (doi:10.1083/jcb.201610048)
6. Davies JA. 2002 Do different branching epithelia use a conserved developmental mechanism? *Bioessays* **24**, 937–948. (doi:10.1002/bies.10161)
7. Iber D, Menshykau D. 2013 The control of branching morphogenesis. *Open Biol.* **3**, 130088. (doi:10.1098/rsob.130088)
8. Metzger RJ, Klein OD, Martin GR, Krasnow MA. 2008 The branching programme of mouse lung development. *Nature* **453**, 745–750. (doi:10.1038/nature07005)
9. Watanabe T, Costantini F. 2004 Real-time analysis of ureteric bud branching morphogenesis *in vitro*. *Dev. Biol.* **271**, 98–108. (doi:10.1016/j.ydbio.2004.03.025)
10. Gjorevski N, Nelson CM. 2011 Integrated morphodynamic signalling of the mammary gland. *Nat. Rev. Mol. Cell Biol.* **12**, 581–593. (doi:10.1038/nrm3168)
11. Villasenor A, Chong DC, Henkemeyer M, Cleaver O. 2010 Epithelial dynamics of pancreatic branching morphogenesis. *Development* **137**, 4295–4305. (doi:10.1242/dev.052993)
12. Davies JA, Hohenstein P, Chang C-H, Berry R. 2014 A self-avoidance mechanism in patterning of the urinary collecting duct tree. *BMC Dev. Biol.* **14**, 35. (doi:10.1186/s12861-014-0035-8)
13. Scheele CL, Hannezo E, Muraro MJ, Zomer A, Langedijk NS, Van Oudenaarden A, Simons BD, Van Rheenen J. 2017 Identity and dynamics of mammary stem cells during branching morphogenesis. *Nature* **542**, 313–317. (doi:10.1038/nature21046)
14. Hannezo E, Scheele CL, Moad M, Drogo N, Heer R, Sampogna RV, van Rheenen J, Simons BD. 2017 A unifying theory of branching morphogenesis. *Cell* **171**, 242–255. (doi:10.1016/j.cell.2017.08.026)
15. Kim HY, Varner VD, Nelson CM. 2013 Apical constriction initiates new bud formation during monopodial branching of the embryonic chicken lung. *Development* **140**, 3146–3155. (doi:10.1242/dev.093682)
16. Nogawa H, Morita K, Cardoso W. 1998 Bud formation precedes the appearance of differential cell proliferation during branching morphogenesis of mouse lung epithelium *in vitro*. *Dev. Dyn.* **213**, 228–235. (doi:10.1002/(SICI)1097-0177(199810)213:2<228::AID-AJA8>3.0.CO;2-I)
17. Affolter M, Zeller R, Caussinus E. 2009 Tissue remodelling through branching morphogenesis. *Nat. Rev. Mol. Cell Biol.* **10**, 831–842. (doi:10.1038/nrm2797)
18. Ewald AJ, Brenot A, Duong M, Chan BS, Werb Z. 2008 Collective epithelial migration and cell rearrangements drive mammary branching morphogenesis. *Dev. Cell* **14**, 570–581. (doi:10.1016/j.devcel.2008.03.003)
19. Greggio C, De Franceschi F, Figueiredo-Larsen M, Gobaa S, Ranga A, Semb H, Lutolf M, Grapin-Botton A. 2013 Artificial three-dimensional niches deconstruct pancreas development *in vitro*. *Development* **140**, 4452–4462. (doi:10.1242/dev.096628)
20. Nogawa H, Ito T. 1995 Branching morphogenesis of embryonic mouse lung epithelium in mesenchyme-free culture. *Development* **121**, 1015–1022.
21. Qiao J, Sakurai H, Nigam SK. 1999 Branching morphogenesis independent of mesenchymal–epithelial contact in the developing kidney. *Proc. Natl Acad. Sci. USA* **96**, 7330–7335. (doi:10.1073/pnas.96.13.7330)
22. Ben-Jacob E, Garik. P. 1990 The formation of patterns in non-equilibrium growth. *Nature* **343**, 523–530. (doi:10.1038/343523a0)
23. Måløy KJ, Feder J, Jøssang T. 1985 Viscous fingering fractals in porous media. *Phys. Rev. Lett.* **55**, 2688. (doi:10.1103/PhysRevLett.55.2688)
24. Lubkin SR, Murray JD. 1995 A mechanism for early branching in lung morphogenesis. *J. Math. Biol.* **34**, 77–94. (doi:10.1007/BF00180137)
25. Family F. 1988 Growth by gradients: fractal growth and pattern formation in a Laplacian field. In *Computer simulation studies in condensed matter physics* (eds D Landau, K Mon, H Schüttler), vol. 33 of Springer Proceedings in Physics, pp. 65–75. Berlin, Germany: Springer.
26. Gerlee P, Anderson AR. 2010 Diffusion-limited tumour growth: simulations and analysis. *Math. Biosci. Eng.* **7**, 385–400. (doi:10.3934/mbe.2010.7.385)
27. Hartmann D, Miura T. 2006 Modelling *in vitro* lung branching morphogenesis during development. *J. Theor. Biol.* **242**, 862–872. (doi:10.1016/j.jtbi.2006.05.009)
28. Short KM *et al.* 2014 Global quantification of tissue dynamics in the developing mouse kidney. *Dev. Cell* **29**, 188–202. (doi:10.1016/j.devcel.2014.02.017)
29. Hirashima T, Iwasa Y, Morishita Y. 2009 Dynamic modeling of branching morphogenesis of ureteric

bud in early kidney development. *J. Theor. Biol.* **259**, 58–66. (doi:10.1016/j.jtbi.2009.03.017)

30. Hirashima T, Iwasa Y, Morishita Y. 2009 Mechanisms for split localization of *Fgf10* expression in early lung development. *Dev. Dyn.* **238**, 2813–2822. (doi:10.1002/dvdy.22108)
31. Menshykau D, Kraemer C, Iber D. 2012 Branch mode selection during early lung development. *PLoS Comput. Biol.* **8**, e1002377. (doi:10.1371/journal.pcbi.1002377)
32. Menshykau D, Kraemer C, Iber D. 2012 Branch mode selection during early lung development. *PLoS Comput. Biol.* **8**, e1002377. (doi:10.1371/journal.pcbi.1002377)
33. Wittwer LD, Croce R, Aland S, Iber D. 2016 Simulating organogenesis in comsol: phase-field based simulations of embryonic lung branching morphogenesis. In *Proc. COMSOL Conf. 2016, Munich, Germany, 12–14 October*. https://www.comsol.com/papers-presentations/2016.
34. Menshykau D, Iber D. 2013 Kidney branching morphogenesis under the control of a ligand–receptor-based Turing mechanism. *Phys. Biol.* **10**, 046003. (doi:10.1088/1478-3975/10/4/046003)
35. Nelson CM, Vanduijn MM, Inman JL, Fletcher DA, Bissell MJ. 2006 Tissue geometry determines sites of mammary branching morphogenesis in organotypic cultures. *Science* **314**, 298–300. (doi:10.1126/science.1131000)
36. Pavlovich A, Boghaert E, Nelson CM. 2011 Mammary branch initiation and extension are inhibited by separate pathways downstream of tgfβ in culture. *Exp. Cell Res.* **317**, 1872–1884. (doi:10.1016/j.yexcr.2011.03.017)
37. Volckaert T, Campbell A, Dill E, Li C, Minoo P, De Langhe S. 2013 Localized fgf10 expression is not required for lung branching morphogenesis but prevents differentiation of epithelial progenitors. *Development* **140**, 3731–3742. (doi:10.1242/dev.096560)
38. Adivarahan S, Menshykau D, Michos O, Iber D. 2013 Dynamic image-based modelling of kidney branching morphogenesis. In *Computational methods in systems biology* (eds A Gupta, Ta Henzinger), pp. 106–119. Lecture Notes In Computer Science, vol. 8130. Heidelberg, Germany: Springer.
39. Dahl-Jensen SB, Figueiredo-Larsen M, Grapin-Botton A, Sneppen K. 2016 Short-range growth inhibitory signals from the epithelium can drive non-stereotypic branching in the pancreas. *Phys. Biol.* **13**, 016007. (doi:10.1088/1478-3975/13/1/016007)
40. Glazier JA, Graner F. 1993 Simulation of the differential adhesion driven rearrangement of biological cells. *Phys. Rev. E* **47**, 2128–2154. (doi:10.1103/PhysRevE.47.2128)
41. Graner F, Glazier JA. 1992 Simulation of biological cell sorting using a two-dimensional extended Potts model. *Phys. Rev. Lett.* **69**, 2013–2016. (doi:10.1103/PhysRevLett.69.2013)
42. Krieg MM, Arboleda-Estudillo YY, Puech P-HP, Käfer JJ, Graner FF, Müller DJD, Heisenberg C-PC. 2008 Tensile forces govern germ-layer organization in zebrafish. *Nat. Cell Biol.* **10**, 429–436. (doi:10.1038/ncb1705)
43. Merks RMH, Perryn ED, Shirinifard A, Glazier JA. 2008 Contact-inhibited chemotaxis in de novo and sprouting blood-vessel growth. *PLoS Comput. Biol.* **4**, e1000163. (doi:10.1371/journal.pcbi.1000163)
44. Wakefield LM, Winokur TS, Hollands RS, Christopherson K, Levinson AD, Sporn MB. 1990 Recombinant latent transforming growth factor beta 1 has a longer plasma half-life in rats than active transforming growth factor beta 1, and a different tissue distribution. *J. Clin. Invest.* **86**, 1976–1984. (doi:10.1172/JCI114932)
45. Graham RL. 1972 An efficient algorithm for determining the convex hull of a finite planar set. *Inform. Processing Lett.* **1**, 132–133. (doi:10.1016/0020-0190(72)90045-2)
46. Onodera T, Sakai T, Hsu JC-f, Matsumoto K, Chiorini JA, Yamada KM. 2010 Btbd7 regulates epithelial cell dynamics and branching morphogenesis. *Science* **329**, 562–565. (doi:10.1126/science.1191880)
47. Daley WP, Matsumoto K, Doyle AD, Wang S, DuChez BJ, Holmbeck K, Yamada KM. 2017 Btbd7 is essential for region-specific epithelial cell dynamics and branching morphogenesis *in vivo*. *Development* **144**, 2200–2211. (doi:10.1242/dev.146894)
48. Lee W-C, Davies JA. 2007 Epithelial branching: the power of self-loathing. *Bioessays* **29**, 205–207. (doi:10.1002/bies.20541)
49. Martin KC, Yuan X, Stimac G, Bannerman K, Anderson J, Roy C, Glykofrydis F, Yin H, Davies JA. 2017 Symmetry-breaking in branching epithelia: cells on micro-patterns under flow challenge the hypothesis of positive feedback by a secreted autocrine inhibitor of motility. *J. Anat.* **230**, 766–774. (doi:10.1111/joa.12599)
50. Köhn-Luque A, de Back W, Yamaguchi Y, Yoshimura K, Herrero MA, Miura T. 2013 Dynamics of VEGF matrix-retention in vascular network patterning. *Phys. Biol.* **10**, 066007. (doi:10.1088/1478-3975/10/6/066007)
51. Ten Dijke P, Arthur HM. 2007 Extracellular control of TGFβ signalling in vascular development and disease. *Nat. Rev. Mol. Cell Biol.* **8**, 857–869. (doi:10.1038/nrm2262)
52. Hinz B. 2015 The extracellular matrix and transforming growth factor-β1: tale of a strained relationship. *Matrix Biol.* **47**, 54–65. (doi:10.1016/j.matbio.2015.05.006)
53. Moore KA, Huang S, Kong YP, Sunday ME, Ingber DE. 2002 Control of embryonic lung branching morphogenesis by the rho activator, cytotoxic necrotizing factor 1. *J. Surg. Res.* **104**, 95–100. (doi:10.1006/jsre.2002.6418)
54. Moore KA, Polte T, Huang S, Shi B, Alsberg E, Sunday ME, Ingber DE. 2005 Control of basement membrane remodeling and epithelial branching morphogenesis in embryonic lung by rho and cytoskeletal tension. *Dev. Dyn.* **232**, 268–281. (doi:10.1002/dvdy.20237)
55. Boas SEM, Carvalho J, van den Broek M, Weijers EM, Goumans M-J, Koolwijk P, Merks RMH. 2018 A local uPAR-plasmin-tgfβ1 positive feedback loop in a qualitative computational model of angiogenic sprouting explains the *in vitro* effect of fibrinogen variants. *PLoS Comput. Biol.* **14**, 1–29. (doi:10.1371/journal.pcbi.1006239)
56. Rens EG, Merks RMH. 2017 Cell contractility facilitates alignment of cells and tissues to static uniaxial stretch. *Biophys. J.* **112**, 755–766. (doi:10.1016/j.bpj.2016.12.012)
57. van Oers RFM, Rens EG, LaValley DJ, Reinhart-King CA, Merks RMH. 2014 Mechanical cell-matrix feedback explains pairwise and collective endothelial cell behavior *in vitro*. *PLoS Comput. Biol.* **10**, e1003774. (doi:10.1371/journal.pcbi.1003774)
58. Poujade M, Grasland-Mongrain E, Hertzog A, Jouanneau J, Chavrier P, Ladoux B, Buguin A, Silberzan P. 2007 Collective migration of an epithelial monolayer in response to a model wound. *Proc. Natl Acad. Sci. USA* **104**, 15988–15993. (doi:10.1073/pnas.0705062104)
59. Reffay M, Petitjean L, Coscoy S, Grasland-Mongrain E, Amblard F, Buguin A, Silberzan P. 2011 Orientation and polarity in collectively migrating cell structures: statics and dynamics. *Biophys. J.* **100**, 2566–2575. (doi:10.1016/j.bpj.2011.04.047)
60. Ouaknin GY, Bar-Yoseph PZ. 2009 Stochastic collective movement of cells and fingering morphology: no maverick cells. *Biophys. J.* **97**, 1811–1821. (doi:10.1016/j.bpj.2009.05.064)
61. Tarle V, Ravasio A, Hakim V, Gov NS. 2015 Modeling the finger instability in an expanding cell monolayer. *Integrative Biol.* **7**, 1218–1227. (doi:10.1039/C5IB00092K)
62. Mark S, Shlomovitz R, Gov NS, Poujade M, Grasland-Mongrain E, Silberzan P. 2010 Physical model of the dynamic instability in an expanding cell culture. *Biophys. J.* **98**, 361–370. (doi:10.1016/j.bpj.2009.10.022)
63. Rolli CG, Nakayama H, Yamaguchi K, Spatz JP, Kemkemer R, Nakanishi J. 2012 Switchable adhesive substrates: revealing geometry dependence in collective cell behavior. *Biomaterials* **33**, 2409–2418. (doi:10.1016/j.biomaterials.2011.12.012)
64. Montesano R, Carrozzino F, Soulie P. 2007 Low concentrations of transforming growth factor-β-1 induce tubulogenesis in cultured mammary epithelial cells. *BMC Dev. Biol.* **7**, 7. (doi:10.1186/1471-213X-7-7)
65. Dougherty ER, Lotufo RA 2003 *Hands-on morphological image processing*, vol. 59. Bellingham, WA: SPIE Press.
66. Guidolin D, Vacca A, Nussdorfer GG, Ribatti D. 2004 A new image analysis method based on topological and fractal parameters to evaluate the angiostatic activity of docetaxel by using the Matrigel assay *in vitro*. *Microvasc. Res.* **67**, 117–124. (doi:10.1016/j.mvr.2003.11.002)
67. Filatov MV, Kaandorp JA, Postma M, van Liere R, Kruszynski KJ, Vermeij MJA, Streekstra GJ, Bak RPM. 2010 A comparison between coral colonies of the genus *Madracis* and simulated forms. *Proc. R. Soc. B* **277**, 3555–3561. (doi:10.1098/rspb.2010.0957)